Magneto-optical system for high speed real time imaging

M. Baziljevich, D. Barness, M. Sinvani, E. Perel, A. Shaulov et al.

Related Articles

Specified value based defect depth prediction using pulsed thermography
J. Appl. Phys. 112, 023112 (2012)

An analytical study of the pulsed thermography defect detection limit
J. Appl. Phys. 111, 093510 (2012)

Profile of the liquid film wetting a channel
Appl. Phys. Lett. 100, 074107 (2012)

A remote scanning Raman spectrometer for in situ measurements of works of art
Rev. Sci. Instrum. 82, 063109 (2011)

Coded excitation for infrared non-destructive testing of carbon fiber reinforced plastics
Rev. Sci. Instrum. 82, 054902 (2011)
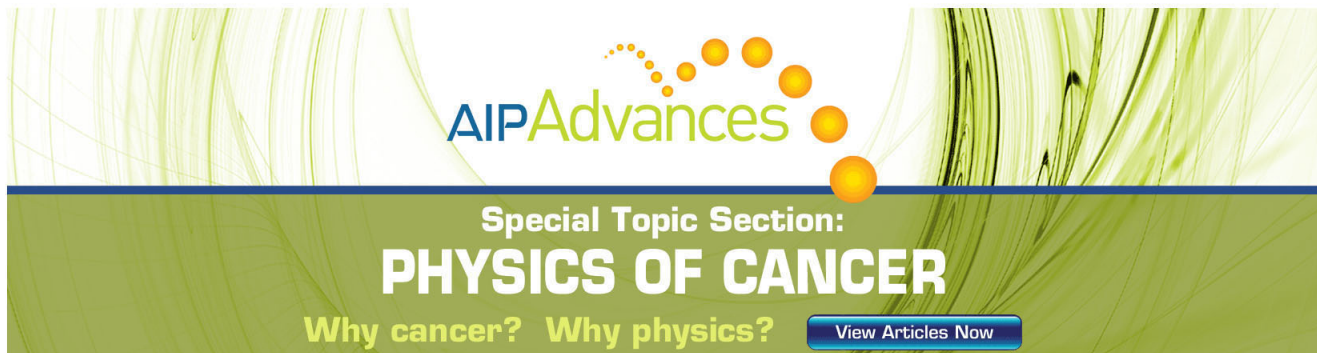
Additional information on Rev. Sci. Instrum.

Magneto-optical system for high speed real time imaging

M. Baziljevich,[a),b)] D. Barness,[c)] M. Sinvani,[d)] E. Perel,[e)] A. Shaulov, and Y. Yeshurun
Institute of Superconductivity, Department of Physics, Bar Ilan University, Ramat Gan, Israel

A new magneto-optical system has been developed to expand the range of high speed real time magneto-optical imaging. A special source for the external magnetic field has also been designed, using a pump solenoid to rapidly excite the field coil. Together with careful modifications of the cryostat, to reduce eddy currents, ramping rates reaching 3000 T/s have been achieved. Using a powerful laser as the light source, a custom designed optical assembly, and a high speed digital camera, real time imaging rates up to 30 000 frames per seconds have been demonstrated. © *2012 American Institute of Physics*. [http://dx.doi.org/10.1063/1.4746255]

I. INTRODUCTION

Magneto-optical (MO) properties of in-plane magnetized bismuth-doped yttrium iron garnet (Bi:YIG) ferrimagnetic crystals enable high quality imaging of magnetic flux distributions in magnetic materials. By using the Faraday rotation of such crystalline plates, mounted in a polarizing microscope or equivalent optical setup, spatial flux distributions can be displayed as a pattern of changing light contrast.[1] Such imaging is non-destructive, local and global, and useful in the entire temperature range from liquid helium to room temperature. The application of these Bi:YIG flux indicators has been particularly successful in the study of flux penetration and current flow in superconducting materials, in the form of crystals, thin films, melt processed and granular samples, and superconducting tapes.[2–5] MO studies have also contributed significantly to our understanding of dendritic flux penetration, thermo-magnetic instabilities and fingering,[6–12] relaxation, vortex lattice melting and the phase diagram of type II superconductors,[13–18] and flux-anti-flux turbulence.[19–22] Refined and optimized for high resolution, the MO imaging technique can even resolve individual vortices.[23–25]

Nearly all MO systems being built so far have used digital CCD cameras or video cameras with frame grabbers for recording, permitting imaging rates up to approximately 30 frames per second (fps). The exception has been the work of Leiderer *et al.*[6,7] where the use of a pulsed laser and optical delay lines (pump-probe technique) enabled the team to take an image a few nanoseconds after heat excitation of the sample. However, their method does not enable real time imaging with consecutive frames.

There are no principal limitations in using the Bi-doped YIG material for fast imaging as the response time of the magnetization alignment is in the sub-nanosecond range.[26,27] The limitations of currently used MO systems are primarily in the image recording rate and ramp rate of the applied field. As a result of these limitations, all the previously mentioned instabilities and flux dynamics can only be investigated in a very limited time window.

This article describes a new magneto-optical system, developed to enable real time imaging at significantly higher rates, to allow studies of flux dynamics on the microsecond scale. The setup also includes custom designed electronics to enable fast ramping of the applied field. A preliminary version of this system has been developed in a framework of a Ph.D. thesis.[12]

II. MAGNETO-OPTICAL IMAGING

Bi-doped YIG is a material with a very strong Faraday effect.[28,29] When linearly polarized light is transmitted through a Bi:YIG crystal, the plane of polarization will be rotated with an angle proportional to the present magnetic field parallel to the direction of light propagation and to the thickness of the crystal. In the case of in-plane Bi:YIG indicator films, the rotation is due to the intrinsic magnetization of the material, which spontaneously aligns with the plane of the film. A perpendicular applied field will tilt the magnetization out-of-plane and produce a component parallel with the beam direction. How easily the magnetization aligns with the applied field, and how soon the rotation saturates, depends on the magnetic anisotropy of the indicator film.[30] By adding a reflective layer to the indicator it can be used in an incident light microscope configuration.[1,2] This also doubles the resulting rotation angle, as the light travels the double length.

The diagram in Fig. 1 shows a typical experimental geometry, with polarized entry and exit beams. The MO indicator chip consists of a transparent gadolinium gallium garnet (GGG) substrate, usually 0.5 mm thick, and the Faraday rotating material itself, which in our case has a thickness of 5 μm. An Al-mirror, approximately 100 nm thick, is deposited to enable the incident light configuration. In addition, the indicator may have a robust protective layer on the mirror and also an anti-reflection coating on the GGG-side of the chip to reduce surface reflection. The indicator is placed on

---

[a)]Author to whom correspondence should be addressed. Electronic mail: michailb@fys.uio.no.
[b)]Permanent address: Department of Physics, University of Oslo, 0316 Oslo, POB 1048, Norway.
[c)]Present address: Elbit Systems Electro-Optics - Elop Ltd., Rehovot, 76111 Israel.
[d)]Present address: Faculty of Engineering, Bar-Ilan University, Ramat-Gan, 52900 Israel.
[e)]Permanent address: Electronics workshop, Bar-Ilan University, Ramat-Gan, 52900 Israel.
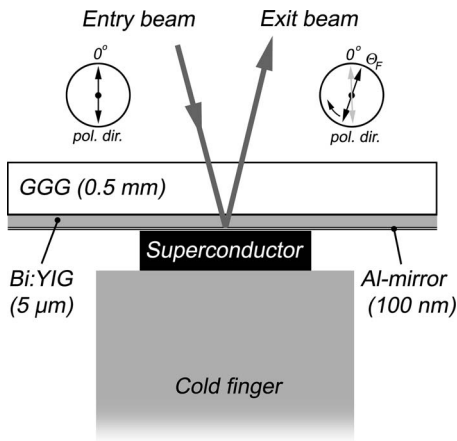
FIG. 1. Diagram showing the geometry of the MO indicator and a sample. Pre-polarized light (relative polarization direction of 0 degrees) first enters the GGG, then the Bi:YIG-layer where it undergoes rotation according to the magnetic field, it is then reflected, and finally exits with a relative Faraday rotation of θ_F.

top of the superconducting sample which is mounted on a cold finger below the window of the cryostat. The polarized beam enters the GGG-side, gets rotated as it travels through the active Bi:YIG film, reflects from the mirror and undergoes a second rotation before it exits the GGG.

To determine the amount of rotation, an analyzer placed in the path of the exit beam is used to produce optical contrast corresponding to the rotation. If the analyzer is crossed relative to the original polarization of the entry beam, and there is no field present, there will be no rotation, and the output from the analyzer will be zero (in principle). However, any field parallel with the beam path will produce a rotation of the entry beam, and this will show up as brightness in the analyzer output, growing in intensity as the field is increased.[31] In a real system, exact polarizer crossing will not produce zero intensity. The ratio between the maximum intensity (open polarizers) and crossed, i.e., the extinction ratio, is a measure of polarizer quality and depolarization in the optical system. Due to this, the optimal image contrast usually requires off-setting the analyzer slightly away from exact crossing.[32]

When the Bi-YIG layer is exposed to a magnetic flux distribution, polarized light will be rotated locally in correspondence with the flux pattern. To image the local variations, and hence the flux distribution, the MO indicator is placed in a commercial polarizing microscope, or as in our case, in a custom made optical system. It is important to note that, in general, the intensity in an MO image will not be linearly related to the applied field. Hence, in every experiment where precise quantitative data are required, a detailed calibration between flux density and camera grey levels must be performed.[3]

III. THE EXPERIMENTAL SETUP

The outline of our MO system follows the basic principles of MO imaging, but with significant modifications as described below. Fig. 2 shows a schematic of the setup.
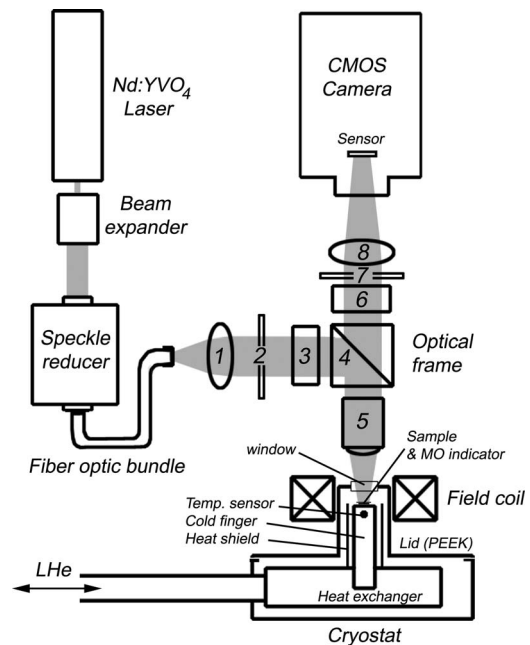

FIG. 2. Schematic of our MO setup. The components in the optical frame are: collimating lens (1), iris (2), polarizer (3), beamsplitter (4), objective (5), analyzer (6), iris (7), imaging lens (8).

A. The light source

An increase in recording speed inevitably results in shorter light exposure per image frame. This defines a critical limit for the maximum recording speed. To be able to expand the range of useful frame rates, the intensity of the light available and the transmission through the optical system must be increased. To meet the requirement of increased intensity we use the green light from a powerful Nd:YVO$_4$ Q-switched laser source (10 ns pulse width) capable of high repetition rates, made by Coherent (Vector 532-1000-20). The laser provides two output wavelengths, the primary at 1064 nm, and a frequency doubled component in the green at 532 nm. The maximal average output, of 1 W at 532 nm (50 μJ/pulse), occurs at 20 000 pulses per second, and drops with increasing repetition frequency to approximately 20 μJ per pulse at 30 kHz. The 1064 nm is currently directed into a beam absorber by a dichroic mirror, but can be used to rapidly heat a sample in future setup modifications.

The laser can be synchronized with the camera, controlling how the pulses will be located in the exposure interval of each frame, or it can run in single shot mode, triggered externally. Synchronization is important, to prevent losing pulses between exposures, as the pulse width is very short.

The Q-switched laser peak-to-peak stability is approximately 40%, which requires inter frame scaling of the camera grey levels during quantitative measurements. This can either be done using a separate photo detector to log stray light from the laser beam, or using parts of the image itself, as a relative grey level indicator. The latter is only possible if there is an area of the image which is unaffected by the sample and its response.

The inclusion of laser light into the optical system produces extensive interference and speckle patterns,

dramatically reducing the image quality. Because of the very short laser pulse duration (10 ns), no simple de-speckling methods like vibrating mirrors or spinning scramble disks can be used. Instead, we employ a commercial device, the SK11 Speckle Reducer from Micro Laser Systems.

The Speckle Reducer uses different lengths of optical fiber, where each fiber differs by more than the coherence length of the laser. The device also works as a beam homogenizer; the input Gaussian intensity profile of the laser is transformed into a homogeneous profile. The SK11 has an entrance aperture diameter of 5 mm, formed by a large number of optical fibers, which after being scrambled inside a chamber, ends up in a flexible 1 meter long fiber bundle. The beam diameter of the laser, initially at 0.25 mm, is increased to 5 mm using a twin lens configuration as a beam expander, to fit the entrance pupil of the SK11, ensuring all fibers are used in fragmenting the laser beam, thus optimizing the decoherence effect on the beam. The light exits in a cone corresponding to a numerical aperture (NA) of 0.2, with barely any visible interference. However, the device introduces a significant loss, transmitting only 35% of the incident power.

The effect of the SK 11 is clearly demonstrated by comparing two test images of the magneto-optical pattern from the magnetic flux code in a regular credit card. To magnify the details, we use a 10 X objective. In the first case, the laser enters the optical system directly. The resulting image quality, presented in Fig. 3(a), is poor and dominated by a strong interference pattern. When the speckle reducer is introduced into the laser beam path, a significant improvement is seen, as demonstrated in Fig. 3(b).

B. The optical system

Even with a powerful laser it is still necessary to ensure that as much light as possible is transmitted through the setup and delivered to the camera sensor. With this in mind, we designed and built an optical frame (see Fig. 2). The cone of laser light emitted by the SK11 de-speckler is semi-collimated by a standard biconvex lens with a focal length of 50 mm, producing an image of the exit tip of the fiber bundle on the back focal plane of the objective, which is a requirement for optimal objective performance. An iris located after the lens is used as an aperture diaphragm balancing brightness and image contrast. As it gets scrambled in the SK11, the laser light loses its linear polarization. A Glan-laser crystal polarizer reintroduces a linear polarization. A high quality coated glass pellicle beamsplitter directs half of the laser beam intensity towards the objective, while the remaining is absorbed by a matted beam block. We use a low strain Plan Apochromat objective from Mitutoyo (5 X, NA: 0.14), with a working distance of 34 mm. After passing through the objective, the light interacts with the Faraday active Bi:YIG layer according to any present magnetic field, and is reflected back into the optical system by the mirror layer on the indicator.

The reflected light re-enters the objective, and is transmitted partly through the beamsplitter. A second Glan-laser polarizer acts as an analyzer, discriminating between different degrees of Faraday rotation in the image. Designed for
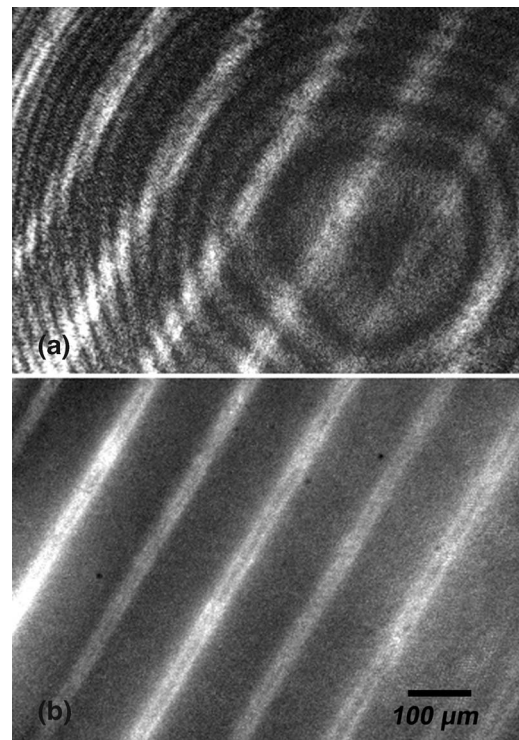

FIG. 3. Comparison of the magneto-optical image quality (a) without and (b) with the speckle reducer introduced into the laser beam path. The magnetic flux distribution in a credit card is used as the test object; the bright stripes are the images of the magnetic code.

infinite optics, the objective projects the image of the sample to infinity. An imaging lens must be included to produce the image, equivalent to a tubus lens in a microscope. In our setup we use a high quality tubus lens from Leica, with a focal length of 200 mm, to image the sample directly onto the camera sensor. A second iris is placed before the imaging lens, to block stray light.

C. The high speed camera and frame synchronization

To record the magneto-optical images we use a Phantom V210 high speed camera from Vision Research. The V210 implements a high quality CMOS sensor chip, with 12-bit signal resolution and a quantum efficiency of 31% at our wavelength. The CMOS technology enables much faster read out speeds compared to the traditional CCD sensors, due to the sensor architecture which favours partial readout. However, they are intrinsically noisier and have smaller dynamic bit ranges. The V210 is capable of 2190 full frame recordings of 1280 × 800 pixels each second. By reducing the frame size, or number of pixels, much higher speeds are available, e.g., a 360 × 240 pixel array can be imaged at 20 000 fps. The camera has 8 GB of memory, and is running on a circular memory mode, which enables very flexible recording. Frames are continuously stored and the earliest recordings erased with the latest. This enables the operator to set a trigger arbitrarily within a full real time running frame sequence of 8 GB. Triggering can be done internally or from an external signal.

FIG. 5. Circuit diagram of the high speed switch for the twin solenoid system. The current power supply I1 feeds the auxiliary pump coil L1 while the field coil L2 stays disconnected. When the S2 electronic switch is activated (and S1 disconnects simultaneously) voltage starts to build up over L1 to a maximum limit. This voltage produces a current through L1 at rate of V/L. The voltage limit is controlled either by an internal voltage limiter (fixed value) in the circuit, or by connecting the variable high voltage supply V1 (trough switch S3). This allows the applied field ramp rate to be varied. Fast insulated gate bipolar transistor (IGBT) switches are used for S1 and S2.
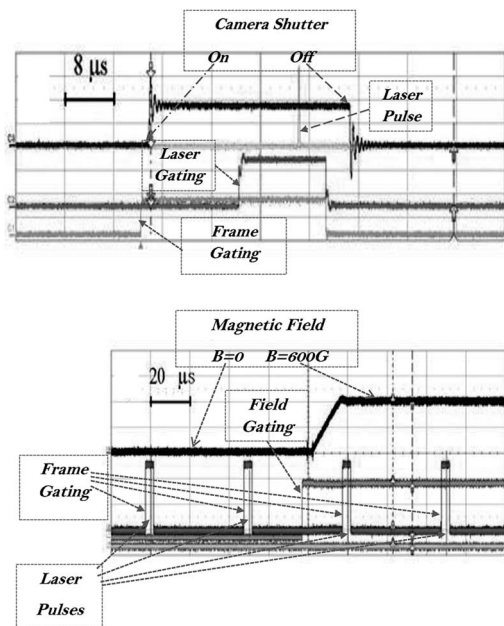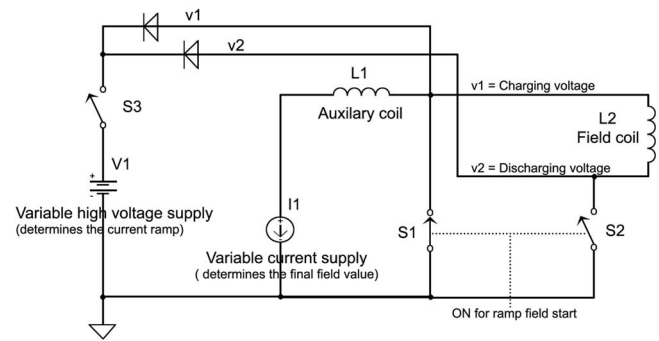
FIG. 4. The frame synchronization scheme: Upper panel: A single camera frame (Camera Shutter) with a single laser pulse within. The laser and frame gating signals are also indicated. Lower panel: A sequence of frames (each containing a single laser pulse) with the external field ramp (Magnetic Field) triggered by a gating signal (Field Gating).

As the laser pulse width is very short (10 ns) it should be synchronized with the camera frames, to avoid losing pulses between the frames, and to ensure that each captured frame is illuminated by the same number of pulses. Preventing the loss of pulses is particularly important if the image exposure time is shorter than the frame interval. At the highest frame rate, each laser pulse illuminates one frame. This synchronization can be done, either by enslaving the laser's Q-switch to the camera's shutter, or by enslaving both to an external triggering source.

In our setup a Tabor 8025 function generator initiates the master trigger which is then distributed by a Delay generator (SRS DG535) to a number of separate, but precisely synchronized output signals, each controlled by an independent delay time. The DG535 is capable of sub-microsecond accuracy and the output signals are monitored by a LeCroy 350 MHz digital scope. The traces in the upper panel of Fig. 4 demonstrate the synchronization scheme for a single camera frame with a single laser pulse within. Indicated in the figure are the triggering events for the laser pulse (marked as "Laser Gating") and the camera shutter (Frame Gating), as well as the actual laser pulse emitted (Laser Pulse) and the camera shutter operation (Camera Shutter). The pulse is clearly located within the duration of the camera exposure time.

An additional trigger from the signal distributor can be used to trigger the current source for the external field. This is important if the entire sequence lasts several milliseconds and one wishes to acquire images while the field is ramped. In the lower panel of Fig. 4 we show a set of exposures (Frame Gating) which were initiated by a master trigger, the trigger that initiates the field ramping (Field Gating), as well as the laser pulses within each frame and the actual magnetic field rise time (Magnetic Field).

D. The applied magnetic field

An important part of high speed dynamic measurements is the ability to apply the external field at ramping rates comparable to the camera frame rates. Hence, a coils system and a special power supply were developed to generate an external magnetic field at a very high ramp rate, with minimum overshoot. However, any rapidly changing coil currents suffer suppression from self-induction and induction induced in the surroundings, resulting in much lower field amplitude or ramp rate. This must be taken into consideration when designing the apparatus.

The basic principle behind the fast ramping technology is the ability to store electric energy in a large auxiliary coil with very high inductance and a high current running through it. Once the coil is charged, an electronic circuit, incorporating high voltage elements, connects the storage coil ($L = 82$ mH) to a field coil with much smaller inductance ($L = 1.7$ mH). The principle scheme is given in Fig. 5.

The rise time of the field coil is determined by the voltage and inductance ratio, allowing a very fast ramping of the current. Our switching power supply uses 37 J of electrical energy stored with a maximal current of 12 A and 1200 V transistors, allowing ramping of the current in the field coil to be as low as 10 μs with a moderate overshoot of less then 10%. At slower ramping rates the overshoot is substantially smaller. This rate can be controlled and decreased by controlling the voltage by a second power supply which lowers the 1200 V at the switch. The field coil is mounted on the cryostat, supplying the external field for the MO experiments. However, this significantly modifies the induction characteristics, as the field from the coil will interact with metal parts of the cryostat.

E. The custom made cryostat

The high ramp rate of the external field induces strong eddy currents in the cryostat or any metallic components located nearby. The induction currents produce a magnetic field

of opposite polarity, relative to the applied field, and reduce the resulting field available to the sample.

The flow cryostat used in our experimental setup was built by Oxford instruments, in principle according to their Microstat He system, but with top loading of the sample and an additional Cernox temperature sensor at the cold finger tip. It is capable of reaching temperatures of 5 K at the heat exchanger, and 7 K at the sample position.

However, several components in the custom made cryostat were fundamentally re-designed to solve the problem with the eddy currents. A schematic description of the cryostat is given in Fig. 2. The cold finger, usually made from copper, was replaced by a sapphire rod. The radiation shield tube around the cold finger was produced with two slits, so any induction current occurring in the tube would be suppressed. Finally, the entire cryostat cover and outer cold finger tube were made from robust PEEK plastic. In addition, using high quality Mitutoyo objectives with very long working distances, we also avoid any induction currents in the proximal metallic tubing of the objective. The remaining parts of the cryostat are well described in documents available from Oxford Instruments, and will not be further elaborated in this article.

IV. SYSTEM PERFORMANCE

A. High speed capabilities

Attached to the cryostat, the applied field solenoid can ramp from zero to 60 mT during 20 μs, which corresponds to a ramping speed of 3000 T/s. This was confirmed in two ways. The power supply has a separate output permitting real time measurement of the current in the field coil. To verify that the field ramp experienced by a sample is fully reflected in the coil current, we introduced a Toshiba TSH118 Hall probe sensor chip into the cryostat. The probe was attached at the sample location on the top of the cold finger and covered by an indicator. The cryostat was cooled to 10 K, to duplicate the experimental conditions. We then checked the temporal profiles simultaneously for the coil current and the Hall voltage, for different ramping times using the LeCroy oscilloscope. Figs. 6(a) and 6(b) show the oscilloscope traces for the coil current and Hall probe signal at 20 μs and 60 μs ramping time, correspondingly. The eddy currents double the ramp duration compared to the coil in free air. There are no significant differences between the coil current and the actual magnetic field ramp inside the cryostat. The spikes seen in the Hall probe traces are electrical disturbances occurring when the high voltage in the power supply undergoes rapid changes, due to switching. They also appear when the driving current to the Hall probe is set to zero, and do not induce any noticeable magnetic field or current in the field coil. We quantify the field overshoot as less than 8% for the 20 μs ramp, and less than 3% for the 60 μs ramp.

Compared to the ramp rate of the isolated twin solenoid system, which can be as short as 10 μs, the reduction is significant but acceptable. The reduction is due to induction currents in the metal parts of the cryostat, which cannot be completely cancelled even with our modifications. Constructing a different coil and adjusting its positions will change the ramp-
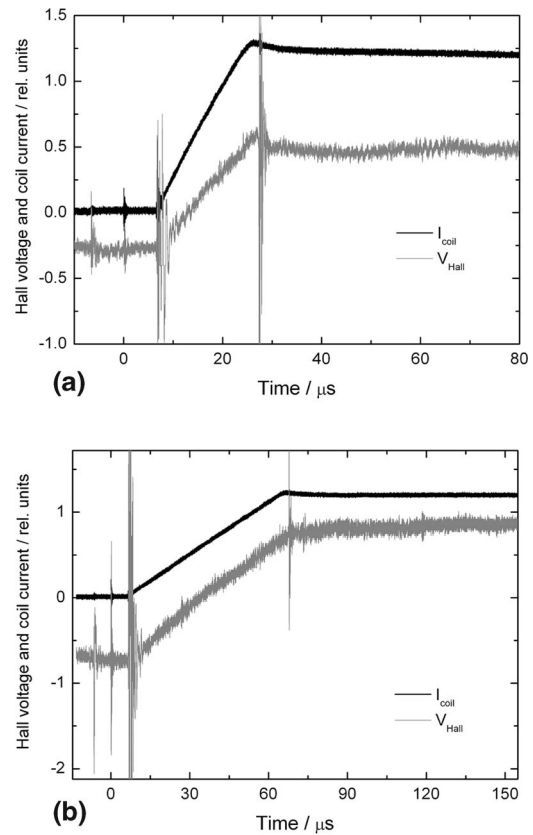

FIG. 6. Oscilloscope traces showing the fast ramping profiles of the coil current and Hall probe voltage at 10 K. (a) Using a 20 μs ramp time, and (b) using a 60 μs ramp.

ing speed, possibly increasing it. Still, the ramp rate we have achieved, together with the speed of the camera, vastly expands the range of high speed MO imaging.

Even with the use of the de-speckling device, there is still some residual interference, originating in the interference between the large numbers of individual fibers in the bundle. It is hard to distinguish from noise in a static image, but is visible if the fiber bundle is vibrated, due to smearing. As the high speed CMOS based camera does not allow for pixel binning, an increase in the frame rate results in a smaller field of view. At 4000 fps, and the laser running at 20 kHz repetition rate, there are 5 laser pulses per frame. This rate produces the maximal energy output. Increasing the frame rate to 20 kfps allows for one pulse per image. At twice this frequency, the energy per pulse (or frame) drops considerably to 20%. This is a significant reduction of photon energy per exposed image and directly translates to reduced image quality.

B. Thermal effects

At maximum laser output power (1 W at 532 nm), the average intensity of the laser light incident on the MO indicator is 20 mW. The reduction is caused by beam transmission through a number of optical components in the setup. However, the intensity is still close to an order of magnitude stronger than in conventional polarization microscopes (with a 100 W Hg-lamp) used in MO systems. Also, one should remember that, unlike conventional MO imaging, the pulses

deposit much higher peak energies in short time intervals. The indicator, as well as any parts of the cold finger which are exposed to the laser will absorb light and increase its temperature. As the superconductor is in contact with these components, one has to consider possible heating effects on the sample. We performed three tests to investigate sample heating.

For this investigation we chose an optimally doped $Bi_2Sr_2CaCu_2O_{8+\delta}$ (BSCCO) single crystal, grown at the University of Tokyo by the group of Tamegai, using the floating zone method.[33] The crystal was cleaved by hand using a bare stainless-steel razor blade, leaving the sample surface flat and shiny face, making it appropriate for magneto-optical imaging. The crystal had rectangular dimensions of 1.9 mm × 1 mm, and a thickness (c-axis) of 50 μm. The critical temperature T_c, approximately verified by monitoring the magneto-optical response of the crystal to a small excitation field, was found to be close to 90 K. The sample was attached to a 0.5 mm thick sapphire disk using C21 paraffin wax, which was then mounted on top of the cryostat cold finger using thermal paste.

The temperature of the crystal was kept constant at 25 K. In all the three tests the sample was saturated with a 60 mT applied field. We then removed the field and let the remnant flux decay due to relaxation for 15 s. In the first case, we run the laser at full power, but have the beam blocked during flux decay. As soon as the laser beam is released an image is taken. In the second test we repeat the experiment without blocking the beam, capturing the image after the 15 s of flux decay. Any possible heating from the laser light would cause the flux to relax faster and result in a weaker trapped flux pattern. In the final test, we have the laser beam unblocked, and run the laser at low intensity. The light incident on the indicator was 0.1 mW, a reduction of 200 times compared to the previous situation. A new image was acquired after the flux decay period of 15 s.

In all the three images there are no significant differences in the trapped flux pattern. We conclude that the thermal heating effect from the intense laser light is marginal. One should remember that most of the light is reflected by the mirror on the back of the indicator. This is the case as long as the beam spot does not extend outside the indicator, as it then could heat the cold finger. Even if we do not find any measurable heating effects in our tests, one should still be mindful of the possibility, in particular if the thermal contact between the sample and cold finger is deficient. The same is the case if the sample is comparably small and acts as a thermal sink for the much bigger indicator. If thermal effects are suspected, a similar test should be performed. Measuring the T_c of the sample by monitoring the MO response to a small field is another optional test for possible thermal heating effects.

C. Preliminary experiments

The BSCCO crystal was used to demonstrate high speed imaging. We zero field cooled the sample to 10 K and exposed it to gradually increasing fields. Also, its response to constant field as the temperature is increased was checked. The crystal
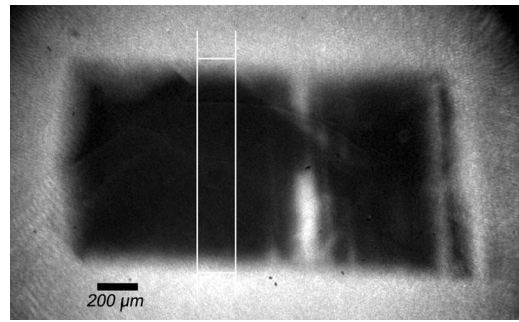

FIG. 7. The image shows flux screening and moderate flux penetration in a zero field cooled BSCCO single crystal at 18 K. The applied field is 50 mT. Dark areas in the image correspond to zero flux. The sample contour can easily be identified, as well as the location of a weak area in the crystal. Detailed flux penetration into the weak area is shown in Fig. 8. The white rectangle defines the measurement region for the flux penetration depth plotted in Fig. 9.

displayed regular flux penetration in the entire sample, except along a weak region/line protruding from both long edges of the rectangular crystal as can be seen in Fig. 7, imaged at 18 K with an applied field of 50 mT. The sample contour is clearly visible due to flux screening. The flux penetration along the weak area is only appearing at fields above 30 mT. Below this, the sample seems to be able to sustain the screening currents and blocking penetration even in the weak region.

After characterizing the MO response of the sample, several different runs were made, increasing the frame rate from 4000 fps to 30 000 fps. In the latter case, the frame size had to be reduced to 256 × 232 pixels, resulting in a smaller field of view. The edge of the sample, where the weak region originates, was chosen as the region of interest. A ramp rate of 1000 T/s was used. At a temperature range of 30–40 K, the flux penetration into the sample along the weak line is sufficiently fast to demonstrate dynamics from frame to frame at a high recording speed, while the pinning of the crystal is strong enough to provide acceptable contrast in the MO images. Fig. 8 shows a time series of gradual flux penetration into the weak region at a recording speed of 30 000 fps. The sample was initially cooled to 35 K, after which a field of 50 mT was applied and kept constant. The first 8 images (a-h) are sampled at 33 μs intervals, and show a tongue of flux penetrating slowly from the sample edge. The last 4 frames (i-l) show the subsequent flux progression at intervals of 330 μs. It is important to note that the entire series shown spans a duration of less than 1.5 ms. If the same experiment were performed on a standard MO setup, and recorded at video rate (30 fps), the sample would be close to fully penetrated even in the first frame of the sequence, i.e., after 33 ms. Our system records 1000 frames during the same interval, and reveals how flux moves into the sample in the initial stage of flux penetration.

A similar experiment was performed at 25 K, with a frame rate of 10 000 fps, to track the flux penetration due to relaxation as a function of time. The temperature and rate was carefully chosen to show clear flux dynamics over a time span of a few seconds, with a suitable field of view (512 × 384 pixels). The crystal was zero field cooled and exposed to an applied field of 30 mT (1 kT/s ramp) which
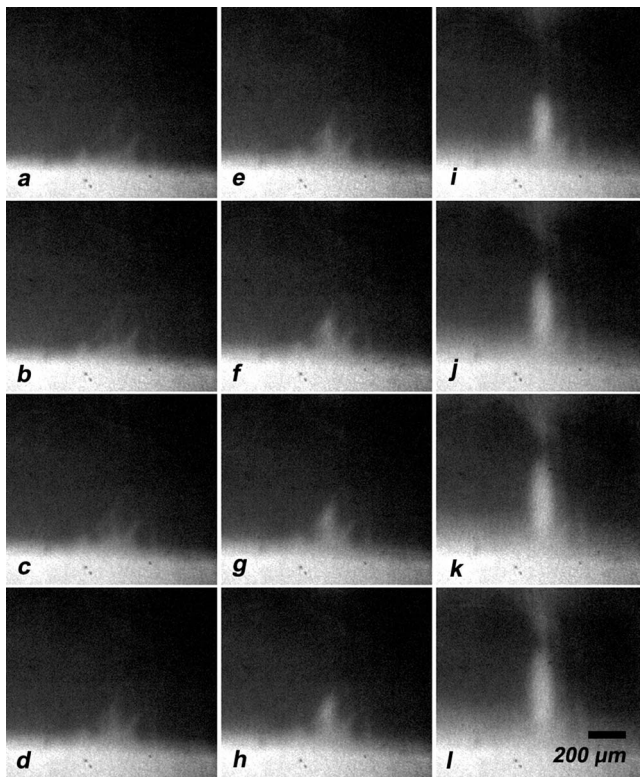
FIG. 8. The image composition shows time series of flux penetration into the weak region of the BSCCO single crystal shown in the previous figure. The sample was ZFC to 35 K, after which a field of 50 mT was applied and kept constant. The recording speed is 30 000 frames per second. The first 8 images (a-h) are sampled at 33 μs intervals, and the last 4 (i-l) at intervals of 330 μs.

was then kept constant. From a time series of more the 20 000 frames, 40 images were selected at certain intervals, to be evenly distributed along a logarithmic time scale and covering more than four decades. From this representative group the flux penetration depths were extracted, defined by the location where the flux front merged with the noise of the flux free central area of the sample. The penetration depth was averaged within the rectangle indicated in Fig. 7. The resulting values were plotted as function of time, on a logarithmic scale, see Fig. 9. The data points require two separate linear
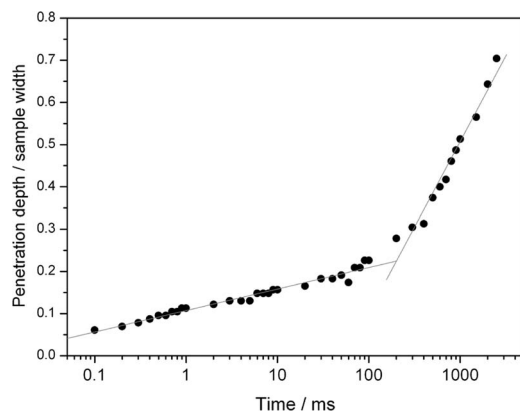

FIG. 9. Plot of the flux penetration depth in a BSCCO single crystal, as a function of time when the applied field is kept constant. The temperature was 25 K, and the applied field 30 mT. The motion of the front is due to flux relaxation.

fits, clearly indicating two different flux relaxation regimes, changing after a relaxation period of approximately 0.2 s. This is an interesting observation, which will be the subject of additional and more extensive investigations in the future.

V. CONCLUSION AND POSSIBLE IMPROVEMENTS

Our newly developed MO setup enables real time imaging at frame rates three orders of magnitude higher than current MO systems. It is also capable of very fast field ramping, at rates exceeding 3000 T/s. Test experiments on a BSCCO single crystal demonstrate MO imaging at 30 000 frames per second, with an acceptable image quality.

At high speed imaging, a reduced frame size results in significant waste of light, as the objective beam spot stays constant. Objectives with higher magnification and larger NA give a smaller spot size of the incident beam, and increased image brightness. This increases the useful frame rate. However, such objectives will have a shorter working distance, possibly affecting the ramp rate of the field due to induction in the nearby metal parts of the objective. The balance between brightness and ramp rate can be tuned to fit the required parameters for a specific sample or material.

To increase the image brightness, the light source itself can also be exchanged with a stronger laser. Another solution, which at the same time will reduce residual interference in the image, is to use multiple inexpensive laser sources. These will not be coherent relative to each other, resulting in a smearing of any interference pattern. An upgrade in intensity will be limited by the number of laser beams which can enter the aperture of the speckle reducer at the same time, and possible thermal effects.

Also, a gradual improvement in the effective field of view comes naturally from the increase in camera speed, due to developments in sensor and readout technology with time. This allows larger sample areas to be observed at the same frame rate and experimental conditions, extending the range of practical experiments.

[1]L. A. Dorosinskii, M. V. Indenbom, V. I. Nikitenko, Yu. A. Ossip´yan, A. A. Polyanskii, and V. K. Vlasko-Vlasov, Physica C **203**, 149 (1992).
[2]M. R. Koblischka and R. J. Wijngaarden, Supercond. Sci. Technol. **8**, 199 (1995).
[3]Ch. Jooss, J. Albrecht, H. Kuhn, S. Leonhardt, and H. Kronmüller, Rep. Prog. Phys. **65**, 651 (2002).
[4]L. S. Uspenskaya, V. K. Vlasko-Vlasov, V. I. Nikitenko, and T. H. Johansen, Phys. Rev. B **56**, 11979 (1997).
[5]M. R. Koblischka, T. H. Johansen, and H. Bratsberg, Supercond. Sci. Technol. **10**, 693 (1997).
[6]V. Bujok, P. Brüll, J. Boneberg, S. Herminghaus, and P. Leiderer, Appl. Phys. Lett. **63**, 412 (1993).
[7]U. Bolz, B. Biehler, D. Schmidt, B.-U. Runge, and P. Leiderer, Europhys. Lett. **64**, 517 (2003).

[8]M. Baziljevich, A. V. Bobyl, D. V. Shantsev, E. Altshuler, T. H. Johansen, and S. I. Lee, Physica C **369**, 93 (2002).

[9]V. V. Yurchenko, D. V. Shantsev, T. H. Johansen, M. R. Nevala, I. J. Maasilta, K. Senapati, and R. C. Budhani, Phys. Rev. B **76**, 092504 (2007).

[10]D. Barness, M. Sinvani, A. Shaulov, T. Tamegai, and Y. Yeshurun, Phys. Rev. B **77**, 094514 (2008).

[11]D. Barness, M. Sinvani, A. Shaulov, C. Trautmann, T. Tamegai, and Y. Yeshurun, J. Appl. Phys. **105**, 07E310 (2009).

[12]D. Barness, Ph.D. thesis, Chap 2.3 (Bar Ilan University, Ramat Gan, Israel, 2009).

[13]A. V. Bobyl, D. V. Shantsev, Y. M. Galperin, T. H. Johansen, M. Baziljevich, and S. F. Karmanenko, Supercond. Sci. Technol. **15**, 82 (2002).

[14]A. Soibel, E. Zeldov, M. Rappaport, Y. Myasoedov, T. Tamegai, S. Ooi, M. Konczykowski, and V. B. Geshkenbein, Nature (London) **406**, 282 (2000).

[15]D. Giller, B. Kalisky, A. Shaulov, T. Tamegai, and Y. Yeshurun, J. Appl. Phys. **89**, 7481 (2001).

[16]S. S. Banerjee, E. Zeldov, A. Soibel, Y. Myasoedov, M. Rappaport, M. Menghini, Y. Fasano, F. de la Cruz, C. J. van der Beek, M. Konczykowski, and T. Tamegai, Physica C **408–410**, 495 (2004).

[17]B. Kalisky, M. Gitterman, B. Ya. Shapiro, I. Shapiro, A. Shaulov, T. Tamegai, and Y. Yeshurun, Phys Rev Lett. **98**, 017001 (2007).

[18]B. Kalisky, Y. Myasoedov, A. Shaulov, T. Tamegai, E. Zeldov, and Y. Yeshurun, Phys. Rev. Lett. **98**, 107001 (2007).

[19]V. K. Vlasko-Vlasov, V. I. Nikitenko, A. A. Polyanskii, G. W. Crabtree, U. Welp, and B. W. Veal, Physica C **222**, 361 (1994).

[20]V. K. Vlasko-Vlasov, U. Welp, G. W. Crabtree, D. Gunter, V. V. Kabanov, V. I. Nikitenko, and L. M. Paulius, Phys. Rev. B **58**, 3446 (1998).

[21]M. R. Koblischka and T. H. Johansen, J. Phys: Condens. Matter **17**, 2723 (2005).

[22]S. Mohan, Y. Tsuchiya, Y. Nakajima, and T. Tamegai, Phys. Rev. B **84**, 180504 (2011).

[23]P. E. Goa, H. Hauglin, M. Baziljevich, E. Il'yashenko, P. L. Gammel, and T. H. Johansen, Supercond. Sci. Technol. **14**, 729 (2001).

[24]M. Terao, Y. Tokunaga, M. Tokunaga, and T. Tamegai, Physica C **426–431**, 94 (2005).

[25]D. Golubchik, E. Polturak, G. Koren, and S. G. Lipson, Opt. Express **17**, 16160 (2009).

[26]A. Zvezdin and V. Kotov, *Modern Magnetooptics and Magnetooptical Materials* (IOP Publishing, Bristol, 1997).

[27]S. E. Irvine and A. Y. Elezzabi, J. Phys. D: Appl. Phys. **36**, 2218 (2003).

[28]P. Hansen, K. Witter, and W. Tolksdorf, Phys. Rev. B **27**, 6608 (1983).

[29]L. E. Helseth, R. W. Hansen, E. I. Il'yashenko, M. Baziljevich, and T. H. Johansen, Phys. Rev. B **64**, 174406 (2001).

[30]H. Ferrari, V. Bekeris, M. Thibeault, and T. H. Johansen, J. Magn. Magn. Mater. **313**, 98 (2007).

[31]Th. Schuster, M. R. Koblischka, H. Kuhn, B. Ludescher, M. Leghissa, M. Lippert, and H. Kronmüller, Physica C **196**, 373 (1992).

[32]P. E. Goa, H. H. Hauglin, Å. A. F. Olsen, M. Baziljevich, and T. H. Johansen, Rev. Sci. Instrum. **74**, 141 (2003).

[33]M. Yasugaki, N. Tokunaga, M. Kameda, and T. Tamegai, Phys. Rev. B **67**, 104504 (2003).